ELSEVIER

Contents lists available at ScienceDirect

## Journal of Power Sources

journal homepage: www.elsevier.com/locate/jpowsour





# Studying voltage losses during discharge for biphenyl-sodium polysulfide organic redox flow batteries

Mohammad M. Bahzad <sup>a,b</sup>, Doug Aaron <sup>a,\*</sup>, Kenneth D. Kihm <sup>a</sup>, Seungha Shin <sup>a</sup>, Umar Saeed <sup>a</sup>, Yu-Kai Weng <sup>a</sup>

- <sup>a</sup> Department of Mechanical, Aerospace, and Biomedical Engineering, The University of Tennessee, Knoxville, TN, 37996, USA
- <sup>b</sup> Kuwait Institute for Scientific Research, 8WP4+7HM, Kuwait City, Kuwait

#### HIGHLIGHTS

- Bp-Na<sub>2</sub>S<sub>x</sub> ORFB is studied by combining polarization and EIS.
- Sodium/sodium ion RE is used for in-situ testing.
- The total voltage loss of both the anode and cathode is measured.
- Sources of voltage loss for both the cathode and anode are identified.
- Bp and Na<sub>2</sub>S<sub>x</sub> half-cells are kinetically limited.

## ARTICLE INFO

#### Keywords: Biphenyl Sodium polysulfide Organic redox flow battery Polarization curve

#### ABSTRACT

Voltage losses during discharge have been quantitatively investigated in a coulombically balanced biphenyl (Bp) sodium-polysulfide ( $Na_2S_x$ ) organic redox flow battery. The individual half-cell electrochemical impedance spectroscopy (EIS) response was studied using a flow cell with an in-situ sodium/sodium-ion reference electrode. The anode, consisting of Bp/Bp $^-$  couple, contributed approximately 58% of the total cell overpotential during discharge. Further investigation revealed that kinetic overpotential dominating both anode and cathode voltage losses during discharge. The EIS response for the sodium-polysulfide half-cell exhibits two semicircles at high and low frequencies. Since there is limited literature relating the high-frequency semicircle to a physical process, this work extends the investigation of cathode high-frequency EIS features using in-situ and ex-situ electrochemical diagnostic tools. The Bp Nyquist plot consisted of a single semi-circle due to its simpler redox reaction relative to the more complicated  $Na_2S_x$ . Tafel analysis was used to calculate exchange current density values, with Bp having a lower exchange current density than  $Na_2S_x$ . This finding explains the relatively higher Bp kinetic voltage loss as compared to  $Na_2S_x$ .

## 1. Introduction

Due to the widespread implementation of intermittent renewable energy, demand for large-scale energy storage systems has increased. Redox flow batteries (RFBs) are promising candidates for large-scale energy storage applications, supporting a wide range of renewable energy sources and improving grid stability [1–4]. One of their main advantages is decoupling energy (electrolyte volume) and power (cell size), making them scalable and suitable for long-duration storage. RFBs can be sorted into two main classifications depending on the type of

electrolyte and/or charge carriers used: aqueous and organic [5-7].

Aqueous RFBs use water-based electrolytes, typically consisting of a combination of metal ions and acids, such as vanadium, iron, and sulfuric acid. Despite the development of aqueous RFBs over the years, their large-scale implementation for utility energy storage has still not been fully realized, mainly because of their low voltage, low energy densities, and relatively low sustainability of materials [8]. For instance, vanadium redox flow batteries (VRFBs), which represent the most mature in aqueous RFBs class, have been demonstrated in several projects [9]. But their low energy density (<25 Wh/L) is the main hindrance

E-mail addresses: mbahzad@kisr.edu.kw (M.M. Bahzad), daaron@utk.edu (D. Aaron).

<sup>\*</sup> Corresponding author.

in their widespread commercialization. Other than VRFBs, numerous aqueous RFBs configurations have also been investigated. These include zinc/bromine [10], all iron [11], and iron/chromium [12]. However, to achieve the goals for RFBs in terms of cost, energy density, and to enable their broad market penetration, extensive research in new electroactive materials is required.

Organic redox flow batteries (ORFBs) have been proposed as an alternative to aqueous systems due to their wider voltage window, high energy density, abundant materials sources, and low cost [13]. These attributes of ORFBs make them attractive for overcoming challenges in grid energy storage. ORFBs utilize organic materials as electrolytes and/or charge carriers; they include organic charge carriers in aqueous electrolytes [14] or inorganic charge carriers in organic electrolytes [15] or can be in total organic combination, normally termed as all-organic RFBs [16]. The disadvantage of ORFBs is low power output due to their low ionic conductivity and mass transport limitations, especially in organic electrolyte system.

Sodium (Na)-based ORFBs are promising due to sodium's high solubility in organic solvents, improving their ionic conductivity [13,17, 18]. One example of Na-based batteries is Na-sulfur (S) batteries, which have been investigated extensively in past decades [19-21]. On the other hand, Na-S battery technology is hindered by low cycle life, high corrosion, and safety concerns because of dendrite formation from Na anode to S cathode, shorting both half cells. To solve these issues, Na metal anodes have been replaced by a liquid electrolyte consisting of biphenyl (Bp) dissolved in organic solvents, such as tetraethylene glycol dimethyl ether (TEGDME), Diglyme, or dimethyl ether (DME) [17,18]. In 2017, Yu et al. tested a Bp Na<sub>2</sub>S<sub>8</sub> battery in a closed cylindrical cell achieving energy density as high as 300 mAh/g<sub>Na2S8</sub> (353 mAh/g<sub>s</sub>) and stable performance for over 700 cycles with limited data on flow cell. Self et al. [17] followed by focusing on Bp|Na<sub>2</sub>S<sub>8</sub> in a flow cell configuration. Their tests resulted in 200 mAh/g<sub>s</sub> capacity with 97% coulombic efficiency. Self et al. [17] achieved lower specific capacity since the polymerization states in that study were limited to soluble states compared to inclusion of insoluble states by Yu et al. [18]. They also showed that kinetic overpotential is a dominant source of overpotential in cathode with no information on anode.

Although recent efforts to explore the electrochemical performance of  $Bp|Na_2S_8$  ORFB are promising, limited information was presented on Bp's in-situ performance compared to sodium-polysulfide  $(Na_2S_x)$ . Therefore, this work extends the research on  $Bp|Na_2S_x$  ORFBs in the following ways: (a) quantifying both half-cell overpotentials for a coulombically-balanced  $Bp|Na_2S_x$  ORFB using an in-situ reference electrode (RE) along with polarization curves, (b) utilizing electrochemical impedance spectroscopy (EIS) to specify the dominant source of overpotential in both anode and cathode, and (c) understanding the high-frequency process of  $Na_2S_x$ .

The anode showed higher voltage loss contribution to full cell total loss, with kinetic overpotential dominating both half-cells. Cathode EIS investigation revealed a high frequency interfacial resistance between the organic liquid electrolyte and ceramic sodium-beta-alumina solid electrolyte (BASE). To the best of our knowledge, this report is the first to study the rate limiting loss of Bp as anode and calculate the relevant kinetic parameters using polarization and EIS as in-situ diagnostic tools. In addition, it contributes to a deeper understanding for processes taking place in the  $\rm Na_2S_x$  half-cell.

#### 2. Materials and methods

## 2.1. Electrolyte preparation

The solvent used in this study was TEGDME (99%, Sigma Aldrich), which was dried using sodium metal flakes and stored over 4 Å zeolite for several days before use [6]. The base electrolyte consisted of 1 molal (m) sodium triflate (NaOT $_{\rm f}$ , 98%, Sigma Aldrich) dissolved in TEGDME. To prepare sodium polysulfide catholyte, sodium sulfide (Na $_{\rm 2}$ S) and

sulfur (S) were mixed at 1:7 M ratio then dissolved in base electrolyte to get charged  $\rm Na_2S_8$  catholyte with dark red color. The anolyte was prepared by dissolving Bp (99.5%, Sigma Aldrich) in base electrolyte and adding excess Na metal flakes to reduce Bp to anion radical, resulting in a dark blue solution. Anolyte was stirred for several days to ensure complete reduction of Bp, then Na metal flakes were removed before adding anolyte to the cell's reservoir. All solutions were stored and prepared in an argon-filled glovebox where oxygen and water concentration were kept below 0.1 ppm.

## 2.2. Cell setup

A bench scale single cell redox flow battery (shown in Fig. 1a–c) was assembled and cycled in an argon-filled glovebox. Two stainless-steel (304, McMaster-Carr) flow plates were machined in house with serpentine flow field (9 channels, 21 mm long, 1 mm wide, and 1 mm deep). Nickel foam (1.6 mm thick, MTI Corp) was used as the electrode for the anode half-cell and carbon felt (CF, SGL Carbon) for the cathode. Both electrodes were compressed by approximately 23% to reduce electronic contact resistance. BASE ( $40 \times 40 \times 1$  mm, Ionotec Ltd.) was used as a separator with butyl rubber gaskets (1.45 mm thick, McMaster-Carr) to seal the cell along with a 1 mm polytetrafluoroethylene (PTFE) gasket around the BASE separator as a support against clamping pressure. Cell bolts were torqued down to 1.5 N-m. Electrodes and BASE geometric surface area were both 4.8 cm². Both electrolytes were pumped into the cell using a single peristaltic pump head (Cole-Parmer) that accepted two lines. Chem-Durance (Cole-Parmer) tubing was used in the

Pump head along with Teflon perfluoroalkoxy alkane (PFA) tubing (McMaster) with polypropylene fittings. Note that for biphenyl, the PFA tubing used to connect the cell to the pump head tubing was stable for short testing periods. PFA tubing is not recommended for sensitive and long tests because biphenyl anion radical reacts with PFA; polypropylene tubing is more stable [17]. In this work, we verified that the rate of interaction between Bp electrolyte and the PFA tubing was small (requiring several hours) compared to the charge transferred during polarization and cycling tests (which takes minutes). While the Bp-PFA interaction did slightly affect SOC during testing, those effects were very small compared to other processes. A photograph of the complete system is shown in Fig. 1a.

To add an in-situ RE, a single cell design was modified to accept a sodium/sodium ion reference electrode (Na/Na $^+$  RE) at the Na-beta-alumina separator (see Fig. 1b-c). This addition is critical to measure the potential of each half-cell; without this RE, investigation is limited to two-electrode measurements that offer relatively little information regarding processes in each half-cell. Another RE (master) can be added to the catholyte or anolyte reservoirs to verify the potential stability of the separator RE. Measurements collected using this 3-electrode setup were stable and reliable, enabling measurement of full-cell performance along with each half-cell performance. Also, EIS can be conducted on the anode and cathode to study their processes separately.

To further study cathode EIS, a symmetric cell was tested with identical CF electrodes separated by Celgard (25  $\mu m$  thick, Celgard© 2325). Both halves were supplied with  $Na_2S_x$  electrolyte from a single reservoir. Other components (flow plate, rubber gaskets, and tubing) for the symmetric cell are identical to the redox flow cell.

#### 2.3. Defining state of charge (SOC)

The theoretical capacity of sodium polysulfide is  $1675 \text{ mAh/g}_s$  for the reduction of S to Na<sub>2</sub>S. At room temperature, S and Na<sub>2</sub>S<sub>4</sub> are insoluble in TEGDME [17,19]. Since all experiments in this work were done at low temperature (26 °C on average), only soluble sodium polysulfide (Na<sub>2</sub>S<sub>x</sub>, where  $5 \le x \le 8$ ) was studied. Na<sub>2</sub>S<sub>8</sub> was thus specified as 100% SOC and Na<sub>2</sub>S<sub>5</sub> as 0% SOC, with 125 mAh/g<sub>s</sub> theoretical capacity. The redox reactions at the anode and cathode are:

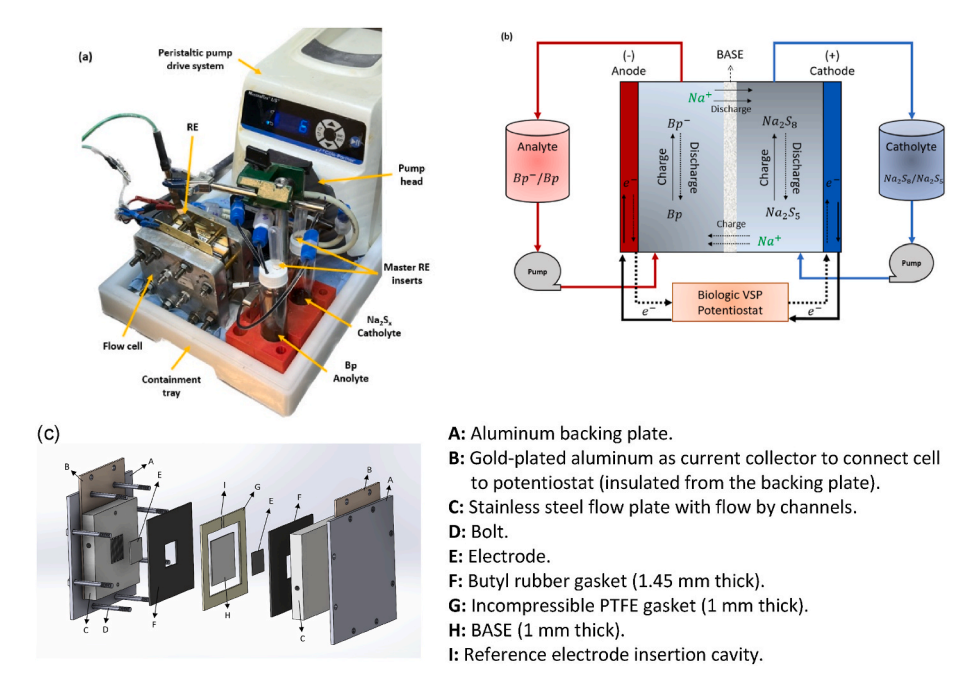
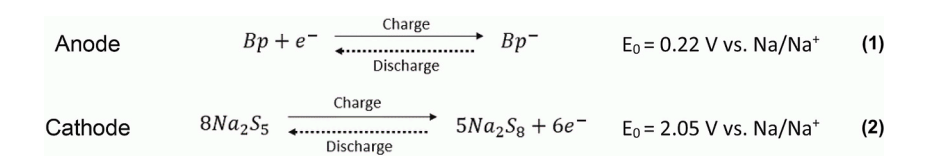


**Fig. 1.** (a) Photograph of the redox flow cell system consisting of two electrolyte reservoirs kept in a 3D printed holder, peristaltic pump, and cell stack all assembled in a PTFE containment tray. (b) Cell illustration. (c) Exploded view of the cell's 3D model showing main components.



## 2.4. Electrochemical characterization

Electrochemical measurements were conducted using a Bio-Logic VSP (BioLogic, France). A 3-electrode cell was used to conduct cyclic voltammetry (CV). The setup consisted of a 30 mL glass vial with a 3D printed lid to seal and hold 3 electrodes. Platinum wire (0.5 mm diameter) was used as working electrode, nickel strip as counter electrode and Na/Na $^+$  as reference electrode. This method was used to measure background current, the reversibility of Bp redox reactions and Bp halfwave potential (E $_{1/2}$ ). The average measured cell temperature during CV tests was 26  $^{\circ}$ C.

Discharge polarization curves were performed at 50% state of charge (SOC) by discharging the cell at constant current for 30 s followed by charging at the same current and for the same period to keep the SOC at 50%. The last 15 s of each potential were averaged, constituting one point on the polarization curve. The same process was repeated at various discharge current values. To monitor the cell SOC, open circuit voltage (OCV) was recorded before and after each run. To perform Tafel analysis, both charge and discharge polarization curves were measured using the same method.

Electrochemical impedance spectroscopy (EIS) tests were conducted on the same full cell with in-situ RE over a frequency range from 5 kHz to 1 Hz. The cell was polarized under constant DC current for 30 s to reach a steady state. Then EIS was measured using 20 mV sinusoidal perturbation amplitude superimposed onto the DC current. This step was repeated several times for different current values to measure EIS for the cell under different polarization conditions. To validate EIS data, Kramer-Kronig was used with an acceptable fit. The BioLogic potentiostat enabled simultaneous collection of both half-cell impedance spectra (i.e., cathode vs. RE, and anode vs. RE).

EIS tests were conducted on a  $Na_2S_x$  symmetric cell. Symmetric cell impedance data were collected between two identical electrodes (cathode vs. anode) with frequency ranging between 5 kHz and 0.1 Hz. Tests for a polarized symmetric cell were conducted using the same process for the full cell.

## 3. Results and discussion

## 3.1. Cyclic voltammetry

CV experiments were conducted using a 3-electrode cell with base electrolyte to measure the background current resulting from impurities in the solution (shown in Fig. 2a). Following a satisfactorily low background activity, 0.1 m Bp anion radical dissolved in base electrolyte (shown in Fig. 2b) was studied. The measured current was normalized by the geometric area of the working electrode (platinum wire) for Fig. 2a and b. When both voltammograms (base electrolyte and Bp anion radical dissolved in base electrolyte) were plotted on the same scale (Fig. 2b), it was apparent that the background current was negligible compared to the current generated by Bp redox reaction.

These CV results confirm that electrolyte drying, storage, and preparation processes were effective since background current is negligible compared to the current generated by active species. In addition, the half-wave potential for Bp ( $E_{1/2}=0.22~V~vs.~Na/Na^+~RE$ ) was calculated from the Bp voltammogram by averaging the anodic (0.266 V) and cathodic (0.175 V) peaks, using Equation (3) [7,22–24]. Half-wave potential of Bp calculated in this study is consistent with the literature [13] because it was crucial for studies in the following sections.

$$E_{1/2} = \frac{E_{pa} + E_{pc}}{2} \tag{3}$$

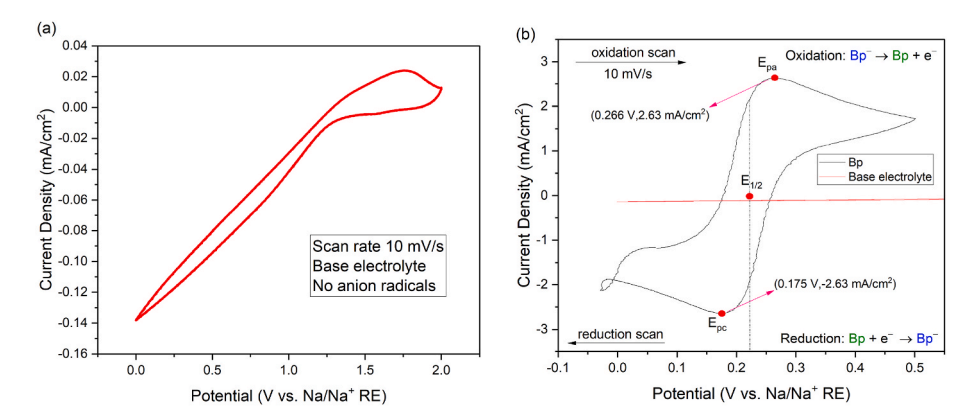


Fig. 2. (a) IR-corrected CV for base electrolyte only. (b) IR-corrected cyclic voltammetry results for 0.1 m Bp anion radical dissolved in base electrolyte and plain base electrolyte plotted on same scale. Platinum wire (0.5 mm diameter) was used as working electrode, nickel strip as counter electrode, and Na/Na $^+$  RE. All tests were conducted in argon-filled glovebox where  $H_2O$  and  $O_2$  concentration were kept below 0.1 ppm.

## 3.2. $Bp|Na_2S_x$ ORFB polarization curve

Prior to conducting polarization studies, the cell was cycled for 22 cycles to ensure the stability and reversibility of electrochemical performance (shown in Figs. S1a-b).

Galvanostatic charge/discharge resulted in high average columbic efficiency of 99.2%, which is comparable to the literature [17,18], indicating the reversibility of redox reactions taking place in the cell. Although durability was not a main target as prior research [17] demonstrated it, we can confirm the durability of the examined cell.

To generate the discharge polarization curve for Bp|Na<sub>2</sub>S<sub>x</sub> ORFB shown in Fig. 3b, the Potentiostat was set up to collect the full-cell voltage (cathode vs. anode) and both half-cell potentials against the Na/Na<sup>+</sup> RE. To verify the RE reading, full-cell voltage was calculated by subtracting the anode potential from the cathode, then comparing to full cell voltage (Fig. 3a). Values agreed to within 8.1 mV (2.2%), confirming the accuracy of half-cell potential readings against RE. Refer to Fig. S2 in the appendix for polarization curve with error bars. Total overpotential ( $\eta_{lotal}$ ) for each curve was calculated by subtracting the operation voltage or potential ( $E_{discharge}$ ) from OCV (Equations (4) and (5)) [7,23].

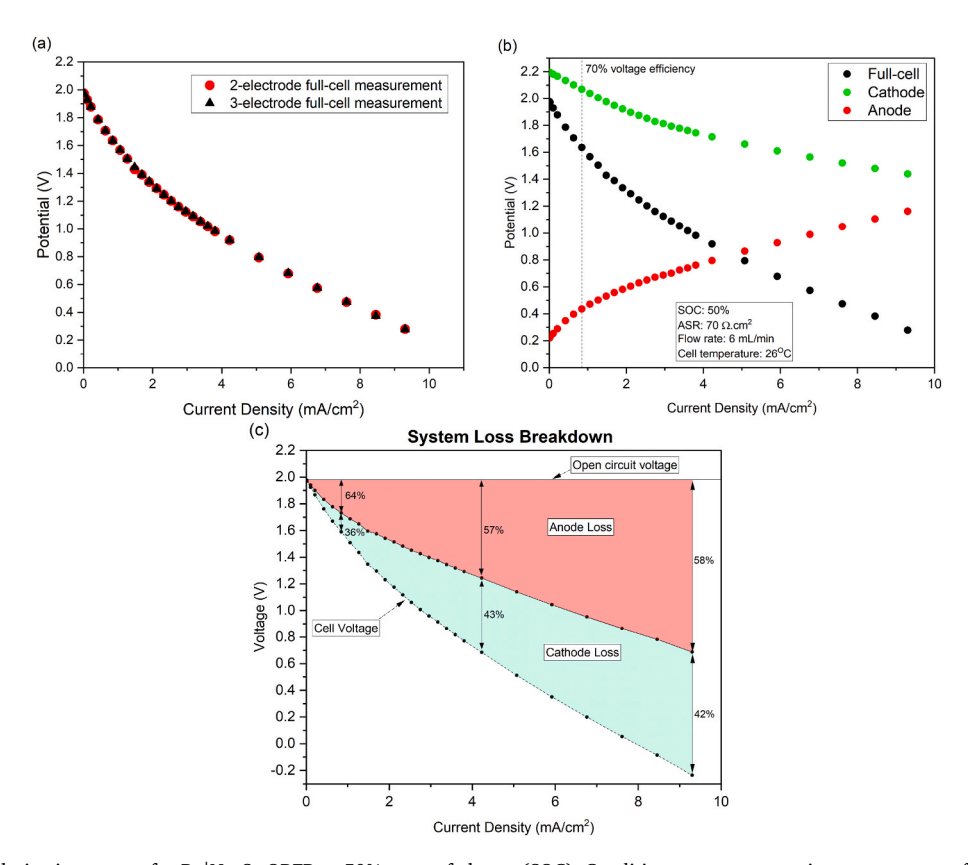


Fig. 3. Experimental polarization curves for Bp|Na<sub>2</sub>S<sub>8</sub> ORFB at 50% state of charge (SOC). Condition: average operating temperature of the cell was 26 °C, area specific resistance (ASR) was  $\sim$ 70 Ohm. cm<sup>2</sup>, flow rate 6 mL/min, 0.13 m Bp, 0.12 m Na<sub>2</sub>S<sub>x</sub>. (a) Comparison between IR-corrected full-cell potential obtained from 2-electrode versus 3-electrode measurements against in-situ Na/Na<sup>+</sup> RE. (b) IR-Corrected polarization curves. (c) Polarization curve with losses isolated from each half-cell using Na/Na<sup>+</sup> RE. Losses included ohmic, kinetic, and mass transport losses, red: voltage losses of anode, green: voltage losses from cathode. The maximum error measured for all polarization curves (full cell and half-cells) is 20 mV (1.5%). (For interpretation of the references to color in this figure legend, the reader is referred to the Web version of this article.)

$$\eta_{total}^{full-cell} = E_{discharge}^{full-cell} - OCV_{full-cell}$$
(4)

$$\eta_{\text{total}}^{\text{half-cell}} = E_{\text{discharge}}^{\text{half-cell}} - \text{OCV}_{\text{half-cell}}$$
(5)

Knowing the overall overpotential of the full cell and for each halfcell, each half cell contribution to the full cell loss (shown in Fig. 3b) was quantified. Over the current density range (0.1–9.3 mA/cm<sup>2</sup>) the anode contributed more strongly to the cell overpotential than the cathode; the anode averaged 58% of the overpotential while the cathode contributed an average of 42%. At low current density (around 70% voltage efficiency), the anode loss accounted for 64% and the cathode 36%, thus the distribution of overpotentials varied slightly over the current density range. As current density increased, the cathode loss increased relative to the anode, reaching 42% at 9.3 mA/cm<sup>2</sup> (which is at the edge of the safe potential window for the electrolyte). Note that current density was calculated by normalizing current by the geometric surface area of electrodes (4.8 cm<sup>2</sup>). A possible explanation for Bp causing higher voltage loss is the nickel foam electrode being less efficient than carbon felt; it might have lower wettability or electrochemical surface area compared to carbon felt. For deeper insight, relevant kinetic parameters will be calculated using Tafel analysis in section 3.4.

## 3.3. Electrochemical impedance spectroscopy (EIS) tests

To break down each half-cell total overpotential into ohmic  $(\eta_{\text{ohmic}}),$  kinetic  $(\eta_{\text{kinetic}}),$  and mass transport  $(\eta_{\text{mt}})$  overpotentials, EIS was conducted under negative DC bias (i.e., discharging the cell) [25,26]. Nyquist plots for each-half cell are shown in Fig. 4a and b. To deconvolute half-cell impedances, their EIS data was fitted to an equivalent circuit model using EC-Lab software.

The anode redox reaction is simpler than that of the cathode; it is a single step, one electron reaction (Equation 1). Thus, its Nyquist plot shows a single semi-circle attributed to charge transfer impedance. A simple Randles equivalent circuit model (shown as inset in Fig. 4a) was used to fit anode EIS data. It consists of a high frequency resistance  $(R_{hf})$ 

in series with a faradaic charge transfer resistance ( $R_{ct}$ ) and a constant phase element (Q) in parallel.  $R_{hf}$  represents the total cell resistance (i.e., contact, liquid ionic, electrode, and separator resistances). The Q circuit element models a non-ideal double layer capacitance at an electrode surface.

The cathode impedance response shows two semi-circles. The first one has previously been attributed to interfacial resistance between solid ceramic separator (BASE) and organic liquid electrolyte [27–29]. The second, lower frequency semi-circle is then related to charge transfer resistance. To account for this extra process, an additional, parallel  $R_{\rm int}Q_1$  element was added to Randles equivalent circuit model (shown as insert in Fig. 4b) and fitted to find resistances values.

Due to the scarcity of literature examining the high frequency response (5 Khz to 45 Hz) of this battery chemistry, a symmetric cell was employed to validate that the first high frequency semi-circle, which is affiliated to interfacial resistance [30–33]. This confirmation was achieved by substituting the ceramic sodium-beta-alumina (BASE) separator with a polymer porous separator (Celgard). When the symmetric cell was subjected to EIS analysis, the initial semi-circle transformed into a straight line (blue curve in Fig. 4c), which is a characteristic response indicating distributed resistance in a porous medium. This alteration serves as evidence that the initial semi-circle corresponds to sodium-beta-alumina interfacial resistance. Notably, the symmetric cell lacking a sodium-beta-alumina separator exhibited a distinct response.

The low frequencies semicircle (<45 Hz) is associated with charge transfer process. To confirm this interpretation, symmetric cell EIS tests were conducted under different cell polarization (shown in Fig. 4d). The high-frequency distributed resistance did not change, whereas the diameter of the semicircle decreased ( $R_{ct}$ ) as discharge current density increased. Thus,  $Na_2S_x$  with Celgard separator has three dominant processes:  $R_{hf}$ , distributed ohmic resistance, and  $R_{ct}$ . On the other hand,  $Na_2S_x$  with BASE (red curve in Fig. 4c) has an additional semicircle, caused by interfacial resistance between liquid electrolyte and ceramic solid electrolyte. This comparison supports the equivalent circuit model used to fit  $Na_2S_x$  data.

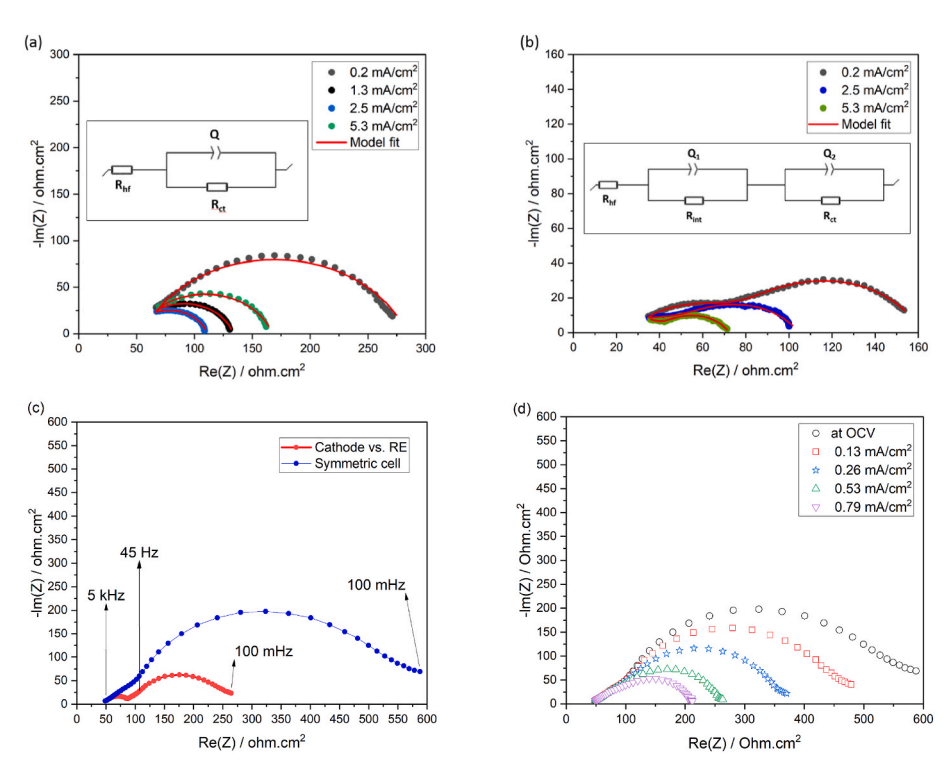


Fig. 4. Nyquist plots for (a) anode and (b) cathode at different cell polarization (discharge current density) between 5 kHz and 1 Hz. Equivalent circuit models shown as insert. (c) Comparison between  $Na_2S_x$  half-cell (cathode versus RE) and a  $Na_2S_x$  symmetric cell (no RE) at OCV. (d)  $Na_2S_x$  symmetric cell at OCV and under different discharge current densities.

Another equivalent circuit model validation tests were carried out; EIS tests were done at different flow rates (0, 6, and 50 mL/min); these tests determine whether the low frequency semicircle might be attributed to mass transport. Nyquist plots at different flow rates are shown in the appendix Fig. S3. These results imply that half-cell impedance between 5 KHz and 1 Hz is mainly caused by reaction-related processes with negligible mass transport effect, further supporting the interfacial and charge transfer resistances assignment.

After fitting EIS data to equivalent circuit models, resistance values were collected. Using Equations (6)–(8) [23,25], ohmic, kinetic, and interfacial (for cathode only) overpotentials at each current density were calculated. The residual overpotential was calculated from subtracting  $(\eta_{ohmic} + \eta_{kinetic} + \eta_{interfacial, cathode})$  from total half-cell overpotential; the residual was assumed to be associated to mass transport.

Total, ohmic, interfacial, kinetic, and residual overpotentials were plotted against discharge current density (Fig. 5a and b). For both half-cells, kinetic overpotential had the largest contribution to cell voltage drop at current density range tested. Findings on cathode losses from this study are consistent with to another study [17], where kinetic losses dominated in Na<sub>2</sub>S<sub>x</sub>, whereas Bp losses were not investigated in previous studies. Thus, these results provide a deeper understanding of Bp|Na<sub>2</sub>S<sub>x</sub> ORFB electrochemical performance.

$$\eta_{\text{ohmic}} = I.R_{\text{hf}} \tag{6}$$

$$\eta_{Kinetic} = \int R_{ct}(I) dI$$
 (7)

$$\eta_{\text{interfacial, cathode}} = I.R_{\text{int}}$$
(8)

Graphite is unsuitable as an electrode option for Bp (anode) due to the reaction between Bp anion radical and carbon, which leads to corrosion. Consequently, nickel foam is used as an electrochemically stable alternative on the Bp side. Several factors contribute to the higher ohmic overpotential observed in the Bp half-cell. These factors include the contact resistance between nickel foam and stainless steel, the stiffness of the electrode impacting the contact, and the observation that SOC influenced ionic conductivity of the electrolyte (with charged Bp anion radical having lower ionic conductivity than the polysulfide electrolyte). Table 1 lists conductivities of different electrolytes and electrodes used in this study.

## 3.4. Tafel analysis

Tafel analysis is an electrochemical tool used to extrapolate exchange current density  $(j_0)$  from Tafel plot and calculate reactions transfer coefficients. Data from the polarization curve at low current density (where kinetic overpotential dominates) were used to generate a Tafel plots (Fig. 6a and b) for both Bp and Na<sub>2</sub>S<sub>x</sub>. From Tafel plots, exchange current densities  $(j_0)$  were extrapolated by fitting a line on the

Electronic and ionic conductivities measured using custom 4 electrode cell. Note: ionic conductivity of base electrolyte is consistent with literature [34].

Conductivity (S/cm)
$1.4\times10^{-3}$
$0.90 \times 10^{-3}$
$0.81 \times 10^{-3}$
1.52
1.82

data with linear increase. Then data were fitted to the Butler-Volmer equation (Equation (9)) [23] to calculate transfer coefficients (i.e.,  $\alpha_f$  and  $\alpha_r$ ). For completely ideal reversible reaction, the sum of transfer coefficients adds up to 1.

Exchange current density of the cathode (0.15 mA/cm²) was higher than the anode (0.09 mA/cm²), which explains the greater kinetic losses in the anode. Similar analysis was performed on  $\rm Na_2S_x$  cathode by Self et al. [17], where they found  $\rm j_0$  to be lower (0.059 mA/cm²). This can be due to many reasons: (i) different electrode material (graphite felt) with different catalytic behavior than carbon felt used in this study, (ii) different solvent used in both studies, which might affect the solvent access to the electrode electrochemical active area, (iii) thinner electrodes, reducing the available area to support reactions. In addition, both half-cell transfer coefficients add up to less than 1 (0.92 for cathode and 0.9 for anode), which can be a result of complex reactions, error associated with EIS data modeling, and measurement error.

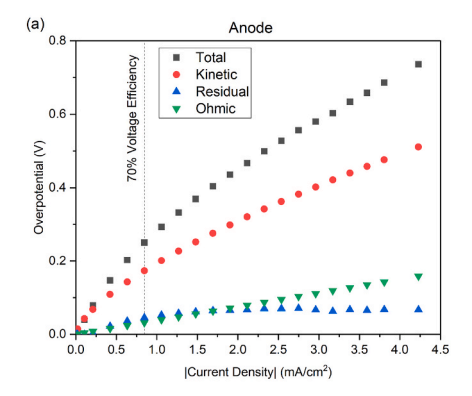
$$j = j_{o} \left[ e^{\left( \frac{\alpha_{e} F}{RT} \eta_{kinetic} \right)} - e^{\left( \frac{-\alpha_{e} F}{RT} \eta_{kinetic} \right)} \right]$$
(9)

#### 4. Conclusions

Table 1

This work demonstrates a technique to quantify voltage loss for each half cell of  $Bp|Na_2S_x$  ORFB during discharge and break down voltage loss into ohmic, charge transfer, interfacial resistance, and mass transport overpotentials. On average, the anode contributed 58% of the cell overpotential over the current density range tested  $(0.01\text{-}9.3~\text{mA/cm}^2)$ . The dominant source of voltage loss in both the anode and cathode is kinetic overpotential. Cathode EIS exhibited a high-frequency process, related to interfacial resistance between the solid BASE and liquid electrolyte. Exchange current density for anode was lower than cathode, explaining the higher voltage loss for Bp relative to  $Na_2S_x$ . These findings address the gaps in the literature in understanding of  $Bp|Na_2S_x$  ORFB.

Current density was calculated by normalizing the current by geometric area of the electrode. This approach is convenient and common in the literature, but it is not an adequate representation since the electrochemical surface area (ECSA) is different than the geometric. In other words, ECSA does not have to scale linearly with geometric area (i.e. you



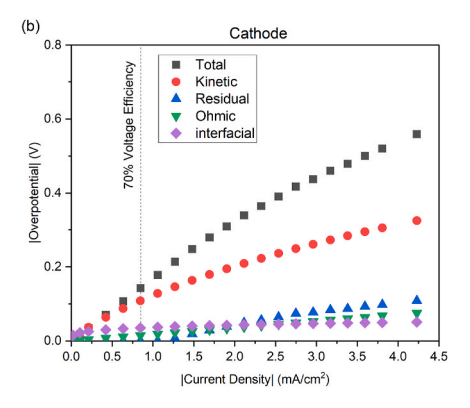
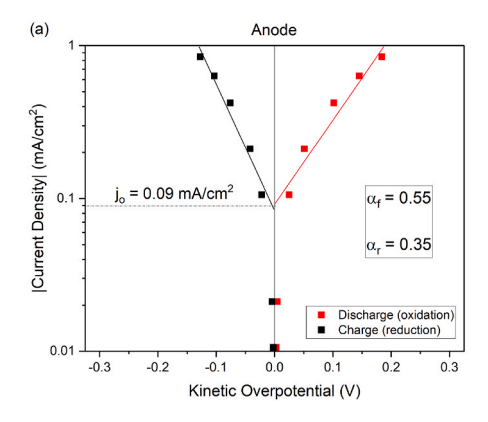


Fig. 5. Breakdown of overpotentials of (a) anode (b) cathode using EIS data.



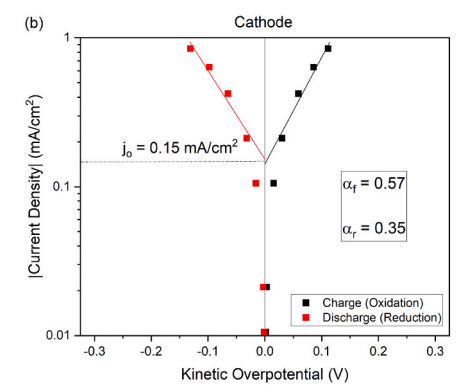


Fig. 6. Tafel plots for (a) biphenyl and (b) sodium polysulfide with kinetic overpotentials during charge and discharge.

can hold geometric area constant while changing ECSA), so polarization studies could use ECSA just like kinetic-specific studies do. For a more accurate representation of electrode performance and ease of comparison to literature, current density should be normalized using ECSA. Our group did not have the resources to conduct experiments to measure ECSA because it is not a trivial process, so we settled for current density based on geometric surface area.

Another limiting factor of this study was Na-beta-alumina solid separator. Because of its fragile nature, only lower compression can be applied to the cell components, leading to high ohmic overpotential. A more durable, thinner, and less expensive separator can improve the performance and practicality of this chemistry of RFBs.

This study's final observation on cathode was that when it's charged pass  $\rm Na_2S_8$  polymerization state (2.25 V OCV), solid sulfur will form and precipitate on carbon felt electrode surface. This phenomenon will cause electrode pores and flow plate channels to clog, raising the pressure between the half-cell inlet and outlet. It is recommended to further investigate the cell pressure drop as cathode polymerization state changes. Higher pressure drops results in higher pump power consumption, which will affect the overall system efficiency. Such a study has not been done by researchers in the field.

We believe this investigation expands the knowledge base on this chemistry of flow batteries. Nonetheless, research and development are still needed for  $Bp|Na_2S_x$  ORFB to compete with other mature energy storage systems. Recommended research areas are:

- 1. Techniques to alleviate kinetic overpotential (i.e., increasing electrode surface area or its catalytic activity) for Bp and  $Na_2S_x$ , since it is the dominant source of voltage loss on for both half-cells. Anode should be prioritized since it has higher impact on the system performance.
- 2. Reduce mass transport overpotential by optimizing flow plate field design, study the effect of flow rate, and synthesizing electrodes with tunned microstructure to reduce diffusion path length.
- 3. Optimize the cell structure to improve its electrochemical performance (i.e., electrode thickness).
- Increase battery current density by reducing ohmic voltage loss through more conductive separator and reducing contact resistance between cell elements.
- 5. Study the effect of cell state of charge effect on catholyte and anolyte flow properties (i.e., pressure drop, viscosity).
- 6. Solvents effect on electrochemical performance of Bp Na<sub>2</sub>S<sub>x</sub> ORFB.

## CRediT authorship contribution statement

Mohammad M. Bahzad: Formal analysis, Investigation, Writing - original draft, Writing - review & editing. Doug Aaron: Supervision, Validation, Funding acquisition, Writing - review & editing. Kenneth D. Kihm: Validation, Writing - review & editing. Seungha Shin:

Validation, Writing – review & editing. **Umar Saeed:** Writing – review & editing. **Yu-Kai Weng:** Writing – review & editing.

## **Declaration of competing interest**

The authors declare that they have no known competing financial interests or personal relationships that could have appeared to influence the work reported in this paper.

## Data availability

Data will be made available on request.

## Acknowledgment

The authors gratefully acknowledge the financial support of the National Science Foundation (award #1933800), which enabled this research work and Kuwait Institute of Scientific Research for supporting Mohammad Bahzad throughout his Ph.D. research work. Special thanks are also due to the Electrochemical Energy Storage and Conversion Laboratory, led by Prof. Matthew Mench, for granting us access to their equipment for our experimental work.

## Appendix A. Supplementary data

Supplementary data to this article can be found online at https://doi.org/10.1016/j.jpowsour.2023.233538.

#### References

- P. Alotto, M. Guarnieri, F. Moro, Redox flow batteries for the storage of renewable energy: a review, Renew. Sustain. Energy Rev. 29 (2014) 325–335.
- [2] P. Leung, et al., Recent developments in organic redox flow batteries: a critical review, J. Power Sources 360 (2017) 243–283.
- [3] A.Z. Weber, et al., Redox flow batteries: a review, J. Appl. Electrochem. 41 (10) (2011) 1137–1164.
- [4] C. Menictas, M. Skyllas-Kazacos, T.M. Lim, Advances in Batteries for Medium- and Large- Scale Energy Storage. Woodhead Publishing Series in Energy, Elsevier Woodhead Publishing, Cambridge, UK, 2014 number 67.
- [5] K. Gong, et al., Nonaqueous redox-flow batteries: organic solvents, supporting electrolytes, and redox pairs, Energy Environ. Sci. 8 (12) (2015) 3515–3530.
- [6] K. Izutsu, in: rev and enlarged (Ed.), Electrochemistry in Nonaqueous Solutions, 2nd, Wiley-VCH, Weinheim, 2009.
- [7] C.G. Zoski, Handbook of Electrochemistry, Elsevier, Amsterdam, 2007.
- [8] Z. Huang, et al., Comprehensive analysis of critical issues in all-vanadium redox flow battery, ACS Sustain. Chem. Eng. 10 (24) (2022) 7786–7810.
- [9] U.S. Department of Energy. Available from: www.sandia.gov/ess-ssl/global-energy-storage-database-home.
- [10] M.C. Wu, et al., Improved electrolyte for zinc-bromine flow batteries, J. Power Sources 384 (2018) 232–239.
- [11] S. Yu, et al., A low-cost sulfate-based all iron redox flow battery, J. Power Sources 513 (2021), 230457.
- [12] Y.K. Zeng, et al., A high-performance flow-field structured iron-chromium redox flow battery, J. Power Sources 324 (2016) 738–744.

- [13] E.C. Self, et al., High-capacity organic radical mediated phosphorus anode for sodium-based redox flow batteries, ACS Energy Lett. 4 (11) (2019) 2593–2600.
- [14] B. Hu, et al., Long-cycling aqueous organic redox flow battery (AORFB) toward sustainable and safe energy storage, J. Am. Chem. Soc. 139 (3) (2017) 1207–1214.
- [15] Q. Liu, et al., Non-aqueous chromium acetylacetonate electrolyte for redox flow batteries, Electrochem. Commun. 12 (11) (2010) 1634–1637.
- [16] Z. Li, et al., Electrochemical properties of an all-organic redox flow battery using 2,2,6,6-tetramethyl-1-piperidinyloxy and N-methylphthalimide, Electrochem. Solid State Lett. 14 (12) (2011) A171.
- [17] E.C. Self, J.L. Tyler, J. Nanda, Ambient temperature sodium polysulfide catholyte for nonaqueous redox flow batteries, J. Electrochem. Soc. 168 (8) (2021), 80540.
- [18] J. Yu, et al., A class of liquid anode for rechargeable batteries with ultralong cycle life, Nat. Commun. 8 (1) (2017) 14629, 14629.
- [19] A. Manthiram, X. Yu, Ambient temperature sodium-sulfur batteries, Small 11 (18) (2015) 2108–2114.
- [20] H. Ryu, et al., Discharge reaction mechanism of room-temperature sodium-sulfur battery with tetra ethylene glycol dimethyl ether liquid electrolyte, J. Power Sources 196 (11) (2011) 5186–5190.
- [21] Y. Wang, et al., Revitalising sodium-sulfur batteries for non-high-temperature operation: a crucial review, Energy Environ. Sci. 13 (11) (2020) 3848–3879.
- [22] N.m. Elgrishi, et al., A practical beginner's guide to cyclic voltammetry, J. Chem. Educ. 95 (2) (2018) 197–206.
- [23] A.J. Bard, L.R. Faulkner, Electrochemical Methods: Fundamentals and Applications, Wiley, New York, 1980.
- [24] R.G. Compton, C.E. Banks, Understanding Voltammetry, second ed., Imperial College Press, London, 2011.

- [25] Y.A. Gandomi, et al., Critical review-experimental diagnostics and material characterization techniques used on redox flow batteries, J. Electrochem. Soc. 165 (5) (2018) A970–A1010.
- [26] M.E. Orazem, B. Tribollet, Electrochemical impedance spectroscopy, in: The Electrochemical Society Series, first ed., Wiley, Hoboken, N.J, 2008.
- [27] F. Sagane, T. Abe, Z. Ogumi, Sodium-ion transfer at the interface between ceramic and organic electrolytes, J. Power Sources 195 (21) (2010) 7466–7470.
- [28] F. Sagane, et al., Li + and Na + transfer through interfaces between inorganic solid electrolytes and polymer or liquid electrolytes, J. Power Sources 146 (1) (2005) 749–752.
- [29] S. Kandhasamy, et al., Operational strategies to improve the performance and long-term cyclability of intermediate temperature sodium-sulfur batteries, Chemelectrochem 8 (6) (2021) 1156–1166.
- [30] A.M. Pezeshki, et al., Elucidating effects of cell architecture, electrode material, and solution composition on overpotentials in redox flow batteries, Electrochim. Acta 229 (C) (2017) 261–270.
- [31] G. Paasch, K. Micka, P. Gersdorf, Theory of the electrochemical impedance of macrohomogeneous porous electrodes, Electrochim. Acta 38 (18) (1993) 2653–2662.
- [32] P.H. Nguyen, G. Paasch, Transfer matrix method for the electrochemical impedance of inhomogeneous porous electrodes and membranes, J. Electroanal. Chem. 460 (1–2) (1999) 63–79.
- [33] Daugherty, M.C., Enhanced Kinetics and Modeling of PAN-Based Carbon Felt Anodes in Vanadium Redox Flow Batteries.
- [34] N.C. Su, et al., Potential complexes of NaCF3SO3-tetraethylene dimethyl glycol ether (tetraglyme)-based electrolytes for sodium rechargeable battery application, Ionics 25 (2) (2019) 541–549.